Journal of Geophysical Research: Atmospheres

RESEARCH ARTICLE

10.1029/2018JD028511

Key Points:

- The squall line was initiated by elevated convection formed in a convergent line when southerly wind intensified above boundary layer
- The southerly wind was enhanced by increasing pressure gradient due to an approaching upstream vortex and strengthened subtropical high
- The jump propagation of the squall line was associated with transition from elevated to surface-based convection

Correspondence to:
Q. Zhang,
qzhang@pku.edu.cn

Citation:
He, Z., Zhang, Q., Zhao, K., & Hu, H. (2018). Initiation and evolution of elevated convection in a nocturnal squall line along the Meiyu Front. *Journal of Geophysical Research: Atmospheres*, *123*, 7292–7310. https://doi.org/10.1029/2018JD028511

Received 12 FEB 2018
Accepted 21 JUN 2018
Accepted article online 2 JUL 2018
Published online 23 JUL 2018

Initiation and Evolution of Elevated Convection in a Nocturnal Squall Line Along the Meiyu Front

Zhiwei He[1], **Qinghong Zhang**[1], **Kun Zhao**[2], **and Huiqin Hu**[3]

[1]Department of Atmospheric and Oceanic Sciences, School of Physics, Peking University, Beijing, China, [2]Key Laboratory for Mesoscale Severe Weather/MOE and School of Atmospheric Science, Nanjing University, Nanjing, China, [3]College of Oceanic and Atmospheric Sciences, Ocean University of China, Qingdao, China

Abstract Observations and analyses from the Variational Doppler Radar Assimilation and Analysis System (VDRAS) were used to investigate the convection initiation mechanism of a nocturnal squall line along the Meiyu Front over central East China on 11–12 July 2014. The squall line occurred on the warm side of the Meiyu Front. The main convection in the squall line was initiated along a mesoscale convergence line above a stable boundary layer at about 2330 local standard time (LST) on 11 July. The convergence line intensified due to enhancement of southerly winds. Momentum budget analyses further revealed that the enhancement of the southerly winds was mainly contributed by an increasing horizontal pressure gradient term, which was associated with the eastward movement of a preexisting mesoscale vortex above the boundary layer and the strengthening of subtropical high. In the early morning of 12 July, a jump propagation of the squall line occurred. As the squall line matured, surface cold pools strengthened due to diabatic heating (most likely evaporative cooling). Then new convection began to initiate in front of the surface cold pools. During the jump propagation of the squall line, the elevated convection in the squall line transitioned to surface-based convection. This is the first study demonstrating the occurrence of elevated convection along the Meiyu Front and its transitioning to surface-based convection by jump propagation.

1. Introduction

There are various classifications of convection, such as classification based on morphology and classification based on organizational modes of convection (Jirak et al., 2003; Maddox, 1980; Parker & Johnson, 2000). Based on the mechanism of its initiation, convection can be classified as surface-based or elevated (Wilson & Roberts, 2006). Elevated convection is convection in which conditionally unstable source air is located above the boundary layer (Glickman & Zenk, 2000). Compared with surface-based convection, elevated convection often poses more challenges to both the research and forecasting communities because it often occurs in areas well removed from surface-based instability (Corfidi et al., 2008), and observations above the boundary layer are much fewer than surface observations. Elevated convection occurs frequently in the United States, especially on the Great Plains (Geerts et al., 2017; Reif & Bluestein, 2017; Wilson & Roberts, 2006), and it tends to occur frequently at night, which may partly account for the nocturnal thunderstorm maximum (Marsham et al., 2011).

Elevated convection was first defined in the pioneering work of Colman (1990a) and Colman (1990b) as convection occurring on the cold side of a surface front or boundary. Subsequent research used a similar criterion (Horgan et al., 2007; Moore et al., 2003). However, in recent years and with the aid of high-resolution observation data and advances in research pertaining to the initiation of convection, the definition of elevated convection changed so that elevated convection was no longer restricted to convection on the cold side of a surface boundary. For example, Wilson and Roberts (2006) defined elevated convection as convection initiation (CI) episodes with no detectable surface convergence in radar or Mesonet data. Reif and Bluestein (2017) found different modes of nocturnal CI events: on a surface boundary, on the cold side of a surface boundary, without a surface boundary, and other modes. According to the definition of elevated convection, CI events on the cold side of a surface boundary or without a surface boundary may be deemed elevated convection. Elevated convection occurring above a stable nocturnal boundary layer has received more attention due to its importance to nocturnal precipitation in the warm season (Parker, 2008; Schumacher & Johnson, 2008). On the Great Plains of the United States, the high occurrence frequency of nocturnal elevated convection has been confirmed by some previous studies: almost 80% of nocturnal CI episodes in the work of Wilson and Roberts (2006) and more than 59% of nocturnal CI events in the work of Reif and Bluestein (2017) (As mentioned above, CI events on the cold side of a surface boundary or without a surface boundary may be deemed elevated convection in the work of Reif & Bluestein, 2017, and these accounted for 59% of nocturnal CI events when combined. CI events in other modes have not been confirmed, so the percentage may be more than 59%.) were found to be elevated. Therefore, the Plains Elevated Convection at Night Field Project (PECAN) (Geerts et al., 2017) was conducted in 2015 to acquire insight into the nocturnal elevated convection over this region and pathways toward improving the relatively poor predicting skill of nocturnal convection in models. In China, however, similar studies have not started yet.

The differences in the CI mechanism between elevated and surface-based convection have been documented in previous studies. Surface-based CI are frequently associated with surface features such as gust fronts, sea breeze fronts, dryline, and terrain effect, whereas elevated convection may be related to convergence features or waves above boundary layer (Weckwerth & Parsons, 2006; Wilson & Roberts, 2006). Apart from CI mechanisms, elevated and surface-based convection are also different in how new cells are continuously initiated to maintain convection systems. In surface-based convection, downdrafts usually reach the surface and form cold pools. In front of these cold pools, conditionally unstable air is lifted by the interaction of the cold surface outflow and vertical wind shear (Rotunno et al., 1988). Different from the case of surface-based convection, there are usually stable layers near the surface in elevated convection; thus, it is often difficult for downdrafts from elevated convection to penetrate the stable layer, reach the surface, and form a cold pool. Therefore, elevated convection requires some other mechanism to continuously initiate new cells to maintain convection systems. Recently, both observations and model simulations have confirmed that systems with no surface cold pool can still generate persistent lifting and initiate new convection cells by generating a wave or bore in stable air (Browning et al., 2010; Marsham et al., 2010, 2011; Parker, 2008; Schumacher, 2009; Schumacher & Johnson, 2008). On the other hand, based on model simulation, Crook and Moncrieff (1988) found that large-scale forcing can initiate and maintain convection without evaporative cooling and cold pools. Before initiation of convection, large-scale convergence can lift the atmosphere to saturation, or close to saturation, over a wide region; after initiation of convection, the large-scale convergence can enhance convection intensity. Therefore, it can be inferred that large-scale forcing may play an important role in at least some elevated convection; however, research pertaining to how this mechanism could work in a real case of elevated convection is still very limited.

The transition between elevated and surface-based convection compounds the challenges of understanding elevated convection (Corfidi et al., 2008; Marsham et al., 2011; Parker, 2008). Studying this transition process is important for better understanding and predicting the evolution of convection systems. Researchers have documented many cases involving the transition process in both observation and simulation. Marsham et al. (2011) reported observation of elevated CI leading to a surface-based squall line in the IHOP_2002 field campaign. The transition process coincided with a reorientation of the squall line. Parker (2008), in an idealized simulation, applied artificial cooling at the rate of 3 K per hour in the low level in surface-based convection, and found that it became entirely elevated when net surface cooling exceeded 10 K. Due to the difference in the mechanisms of the two kinds of convection, the convection systems would exhibit different characteristics before and after the transition. For instance, Wilson and Roberts (2006) found a difference in life span between elevated and surface-based convection. Storms that did not produce gust fronts (outflow boundaries of cold pool) often lived 2–6 hr, whereas those that did produce these frequently lived at least 8 hr. Therefore, it is inferred that this transition from elevated convection to surface-based convection may contribute to the long life span of some elevated-initiated convective systems (Marsham et al., 2011). Another reason why the transition between elevated and surface-based convection is important is because it can affect not only the subsequent evolution of convection systems but also their tendency to produce severe weather. Because it is difficult for downdrafts from elevated convection to reach the surface, elevated convection tends to be associated with a reduced likelihood of producing significant severe winds and tornadoes (Horgan et al., 2007).

In China, there has been much less research on elevated convection than in the United States. Previous research focused mostly on the synoptic condition of elevated convection in cold seasons (Wu et al., 2013; Zhang et al., 2014), and there have been few studies on elevated convection in the warm season. However, it has been revealed that there is a significant nocturnal peak of mesoscale convective systems (MCSs) in the warm season in central East China, and these nocturnal MCSs are closely associated with the

Meiyu Front (He et al., 2016). As a frontal zone characterized by intense equivalent potential temperature gradient at 850 hPa (Y. Zheng et al., 2008), the Meiyu Front seems to play different roles in the initiation of these nocturnal MCSs compared with surface fronts. Whether convection in these nocturnal MCSs along the Meiyu Front is elevated is an interesting question, but the answer has remained elusive due to the limitation of observation. Fortunately, during Intensive Observation Period 8 (IOP8) of the Chinese 973 Program "Observation, Prediction, and Analysis of severe Convection of China" (OPACC; Xue, 2016), one nocturnal squall line along the Meiyu Front on 11–12 July 2014 in central East China was captured during the field campaign. Radar and dense surface station observations provided an opportunity to study its detailed initiation mechanism and confirm whether this squall line was elevated.

This study investigated the CI mechanism and evolution of a nocturnal squall line along the Meiyu Front on 11–12 July 2014 in central East China. The remainder of this paper is organized as follows. Section 2 introduces the data and methodology, and section 3 describes the synoptic background. The mechanism of CI is explored in section 4. A conclusion is presented in section 5.

2. Data and Methodology

2.1. Observation Data From the Field Campaign

The squall line of this work was observed in IOP8 of the Chinese 973 Program OPACC. The field experiments in IOP8 were carried out on 11–12 July 2014 over central East China, where observation instruments including automatic weather station (AWS), sounding, wind profile radar, Doppler radar, distrometer, radiometer, and other instruments were deployed. The data used in this work were mainly AWS and Doppler radar observations.

The evolution of this squall line was captured by composite radar reflectivity (Figure 1). Linear convection was initiated at 2330 local standard time (LST) on 11 July, and a squall line then formed (solid lines in Figures 1a and 1b). In the early morning of the next day, a jump propagation of the squall line was observed (dashed line in Figure 1c). This process occurred through the generation of new linear convection and the formation of a new squall line in front of the original one, while the old squall line weakened gradually and dissipated into stratiform echoes (Figures 1c and 1d). New cells first initiated to the southwest of the original squall line (in the box in Figure 1c around 0200 LST 12 July, not shown here) and then gradually formed a new squall line to the south. Similar discrete propagation of squall line has been documented in the work of Fovell et al. (2006). The detailed mechanisms responsible for the jump propagation will be discussed and compared with the work of Fovell et al. (2006) in section 4.3.

2.2. Data Assimilation System

To incorporate the large amount of data obtained from the field campaign with model data, the Variational Doppler Radar Assimilation and Analysis System (VDRAS) developed by the National Center for Atmospheric Research (NCAR) was used to blend the surface observation and radar data with mesoscale model output to obtain high-resolution analyses of wind, temperature, humidity, and cloud parameters (X. Chen et al., 2016; Sun, 2005; Sun et al., 2010; Sun & Crook, 1997, 1998; Tai et al., 2011). The VDRAS was developed to retrieve meteorological variables by assimilating observations from single or multiple Doppler radars (radial velocity and reflectivity) based on a 4DVAR scheme and a cloud-scale model with warm rain microphysics. Other observations such as those of radiosondes, profilers, and surface networks are assimilated into VDRAS through an objective analysis method prior to 4DVAR radar assimilation. Soundings extracted from the mesoscale model, which was the Weather Research and Forecasting (WRF) model in this work (Skamarock et al., 2008), were used to provide the background analysis for data assimilation. The aforementioned literature includes additional details about VDRAS.

2.3. Model Configuration

As introduced above, VDRAS combines surface observation, the WRF model, and Doppler radar to generate high-resolution analyses. The domains of the WRF model and VDRAS analyses are shown in Figure 2. Two nested domains with a horizontal resolution of 9 and 3 km, respectively, and 40 vertical layers were configured in the WRF model (version 3.6.1). The WRF model was initiated at 0800 LST 11 July 2014 and ended at 0800 LST 12 July 2014 with the National Centers for Environmental Prediction (NCEP) final

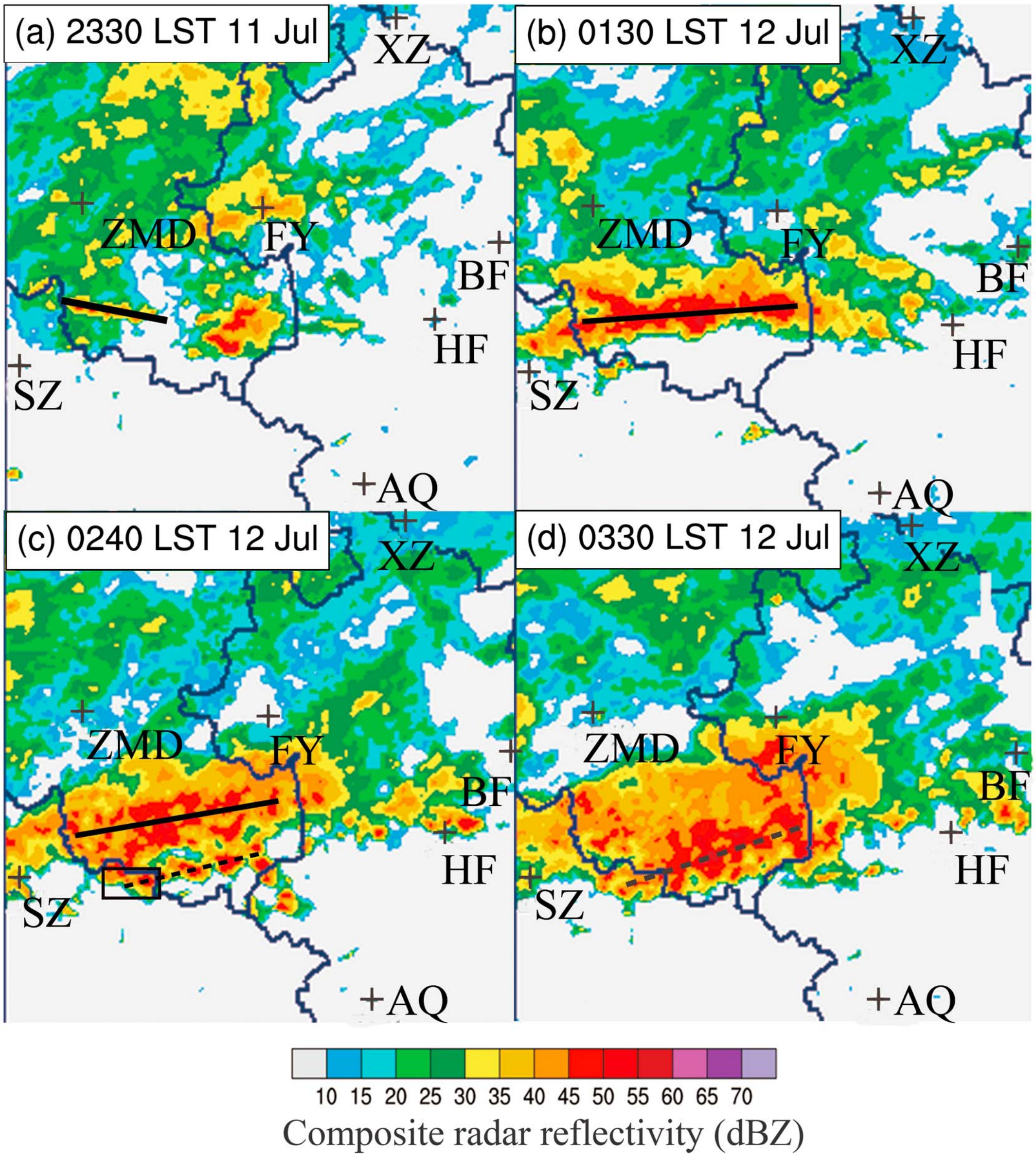

Figure 1. (a–d) Mosaics of composite radar reflectivity on 11–12 July over central East China. The time of each subfigure is marked at the upper left (local standard time, LST). The black solid line represents the long axis of the squall line, and the dashed line in (c) and (d) represents the newly formed squall line that developed when the jump propagation occurred. The crosses in the figure represent Doppler radars in the region. The box in (c) shows the location where new cells first initiated around 0200 LST 12 July when jump propagation began.

(FNL) reanalysis data (see http://rda.ucar.edu/datasets/ds083.2/ for more details) as the initial and boundary conditions.

The surface observation data used in this study were observations from 2,712 AWSs at an interval of 1 hr (Figure 2). The data of six S-band Doppler radars distributed around the squall line of interest were assimilated into the VDRAS system (Figure 2). The VDRAS analyses had a horizontal resolution of 3 km and a vertical resolution of 300 m starting from the bottom layer of 150 m. The length of 4DVAR cycle is set to 10 min in this work, during which the radar and surface data within the window are assimilated and an optimal analysis is obtained by minimizing the cost function, which measures the misfit between the model variables and the observations (Sun & Crook, 2001). At the end of each cycle, the output of final analysis is obtained, so the output interval in this work is also 10 min. The analyses started at 1700 LST on 11 July 2014 and ended at 0800 LST on 12 July 2014.

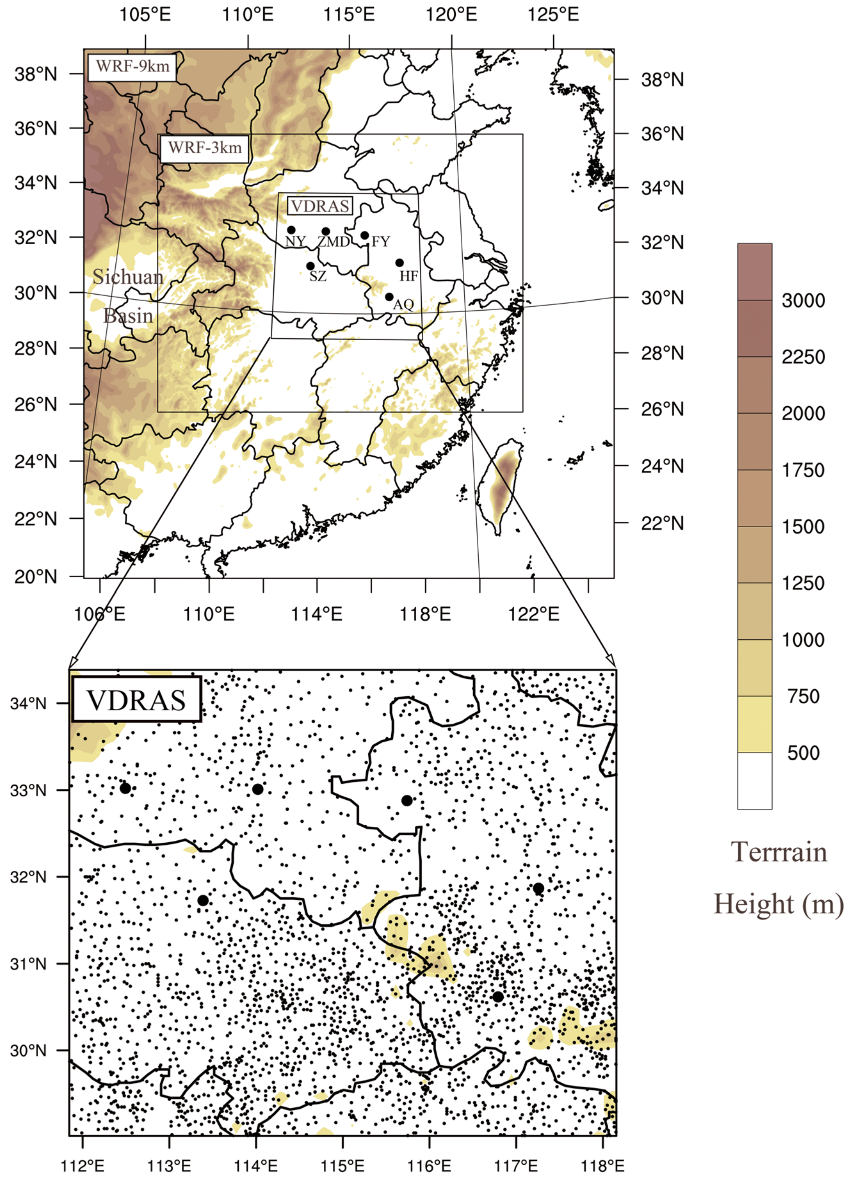

Figure 2. Domain of the Weather Research and Forecasting (WRF) model and terrain heights (shading, unit: m). The Lambert map projection is applied in the WRF domain. The whole region is the outer domain of the WRF model (9 km), and the middle box is the inner domain of the WRF model (3 km). The innermost quadrangle represents the domain of Variational Doppler Radar Assimilation and Analysis System (VDRAS). The equivalent cylindrical map projection was applied in VDRAS, so its domain is not rectangular on the Lambert-projection map. The large black dots represent the assimilated radar stations. The small black dots in the zoomed-in VDRAS domain represent automatic weather stations (AWSs).

3. Synoptic Background

Figure 3 shows the variation of the synoptic background at different levels. The data are from the ERA 5 reanalysis data (see https://www.ecmwf.int/en/forecasts/datasets/archive-datasets/reanalysis-datasets/era5 for more details). The squall line was on the northwestern edge of the subtropical high, and the upstream trough was very weak at 500 hPa (Figures 3a, 3c, and 3e). As a result of water vapor transport by southerly winds on the west edge of the subtropical high at the low-level troposphere and a minimal change in the water vapor aloft, a high precipitable water tongue extended from the South China Sea to central East China. The squall line occurred in the region where the humidity gradient was large and the PW reached as high as 50–60 mm.

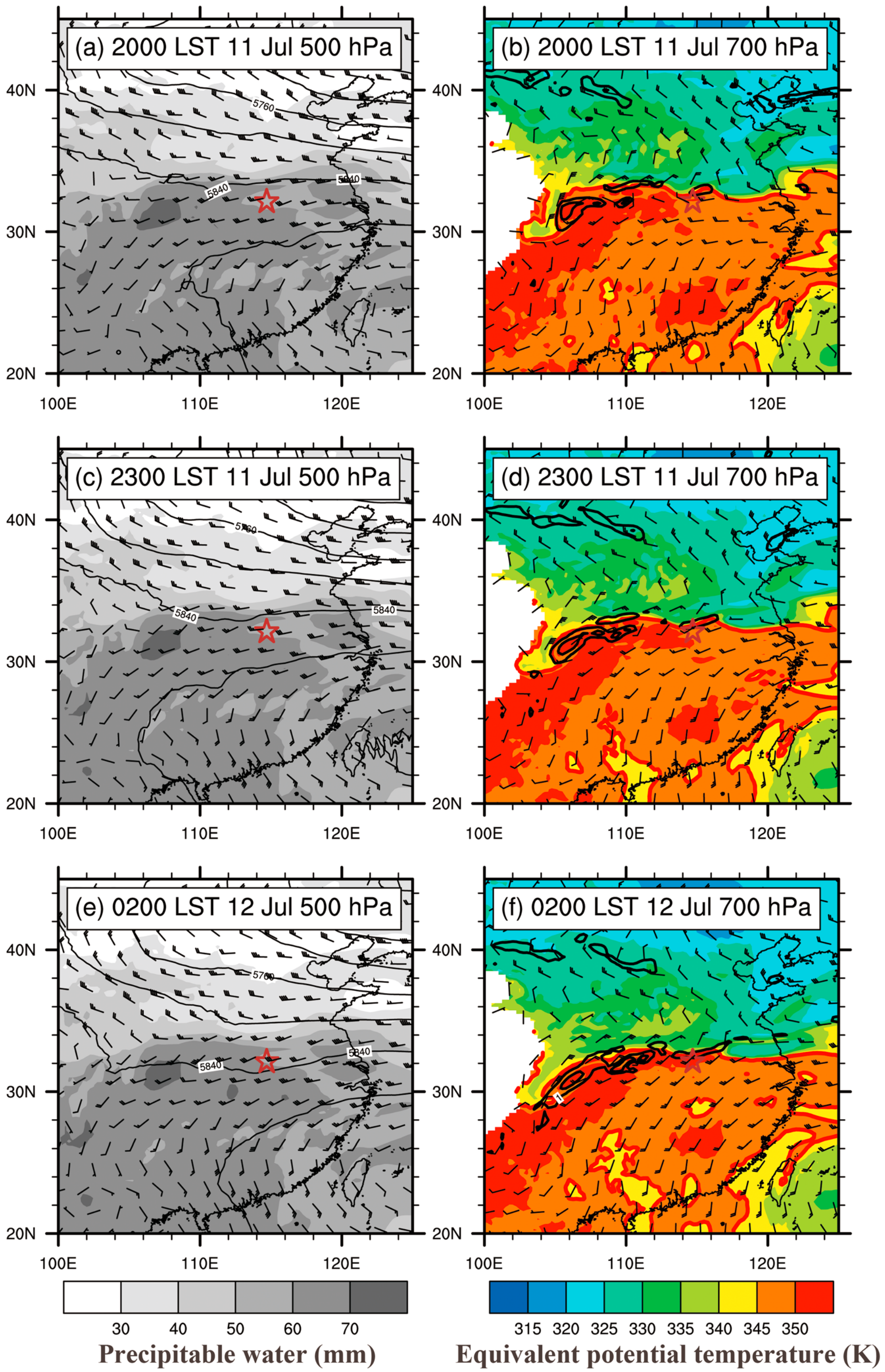

Figure 3. Variation of the synoptic circulation background with time at 500 and 700 hPa. The time and level of each subfigure are marked at the top left. Parameters plotted include geopotential height (black contours, gpm), winds (wind barb, a full barb represents 4 m/s) at 500 hPa, and precipitable water (shading, mm) in (a, c, and e) and equivalent potential temperature (shading, K), winds (wind barb, a full barb represents 4 m/s), and vorticity (black contours, unit: 10^{-4}/s; only values greater than 10^{-4}/s are plotted at the interval of $10^{-4} s^{-1}$) at 700 hPa in (b, d, and f). The contours of 345-K equivalent potential temperature are highlighted as red, thick contours in (b, d, and f). The brown stars in each subfigure represent the location where the squall line initiated. Variable values are removed in (b, d, and f) where elevation is higher than 700 hPa. The data are from ERA 5 reanalysis data.

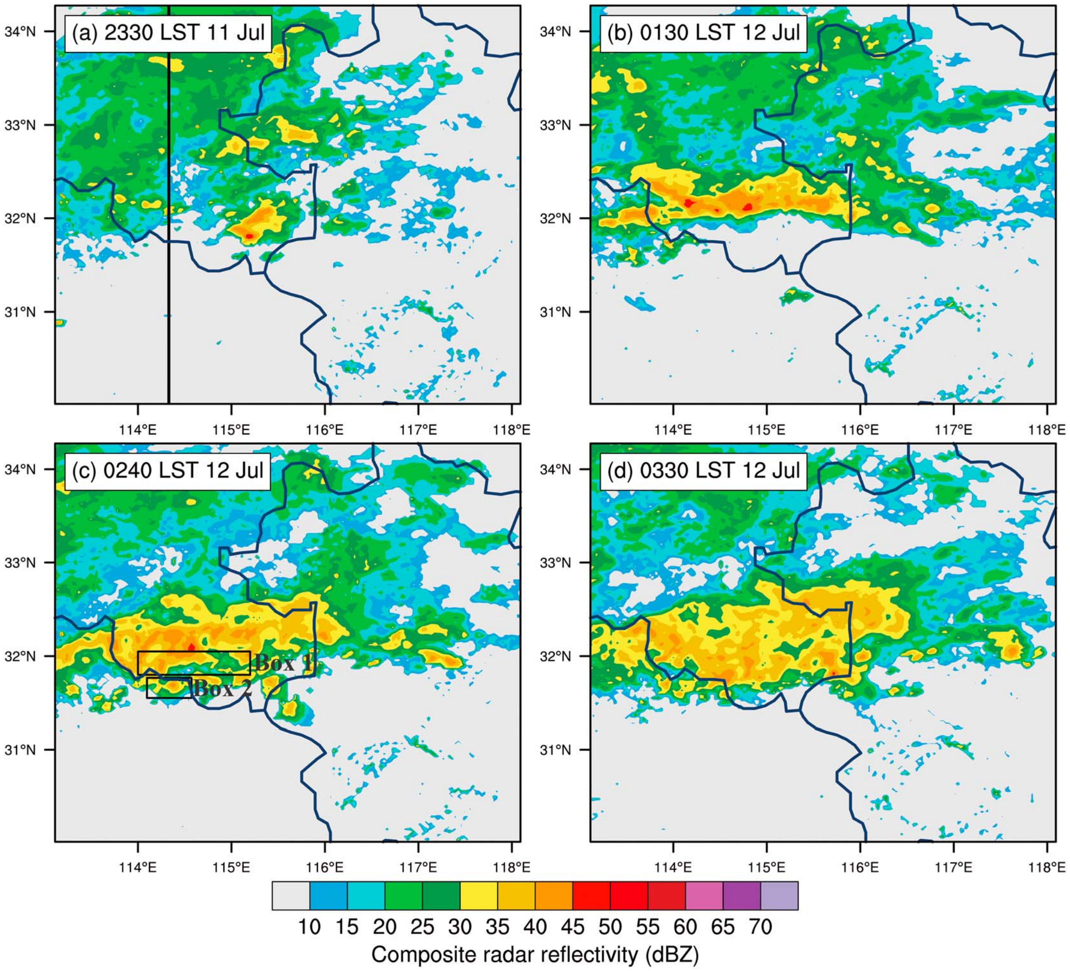

Figure 4. VDRAS-simulated composite radar reflectivity (unit: dBZ). The time of each subfigure is marked at the upper left. The north-south oriented black line in (a) shows the location of the cross-sections in Figure 5. The Box 1 in (c) shows the region for temperature budget analysis in Figure 13. The Box 2 in (c) is the same as that in Figure 1c, which shows the location where new cells first initiated when jump propagation occurred.

An important feature observed at 700 hPa (Figures 3b, 3d, and 3f) was the eastward movement of a vortex from 2000 LST 11 July to 0200 LST 12 July (represented by the center of cyclonic vorticity in Figures 3b, 3d, and 3f). The vortex featured cyclonic circulation was significant at 700 hPa, but not clear at 500 hPa. This type of vortex is observed frequently in southwest China in the warm season and is often termed as southwest vortex (SWV) by the forecasting community (Z. Chen et al., 2003; Fu et al., 2011). The SWV usually forms to the east of the Tibetan Plateau in the Sichuan Basin, moves eastward, and acts as an important trigger of torrential rainfall. In this case, the SWV moved from southwest China at 2000 LST on 11 July to central East China at 0200 LST on 12 July. There was a low pressure center in the northeast of China at 700 hPa at 2000 LST 11 July (not shown here), to the southwest of the low pressure system was northerly winds. The northerly winds converged with southerly winds to the northwest of subtropical high in central East China, forming an east-west oriented convergence line. This convergence line, accompanied by cyclonic vorticity, extended from the SWV to central East China (Figure 3b). There was significant humidity contrast between the northern and southern sides of the convergence line, corresponding to a sharp gradient of equivalent potential temperature. The dense equivalent potential temperature contours indicated the approximate location of the Meiyu Front (Y. Zheng et al., 2008). Following the work of Luo et al. (2014), we took the 345 K equivalent potential temperature contour to represent the Meiyu Front. The squall line was initiated on the warm side of the Meiyu Front. This is different from previous research, which found that elevated convection usually occurs on the cold side of surface fronts (Horgan et al., 2007; Moore et al., 2003).

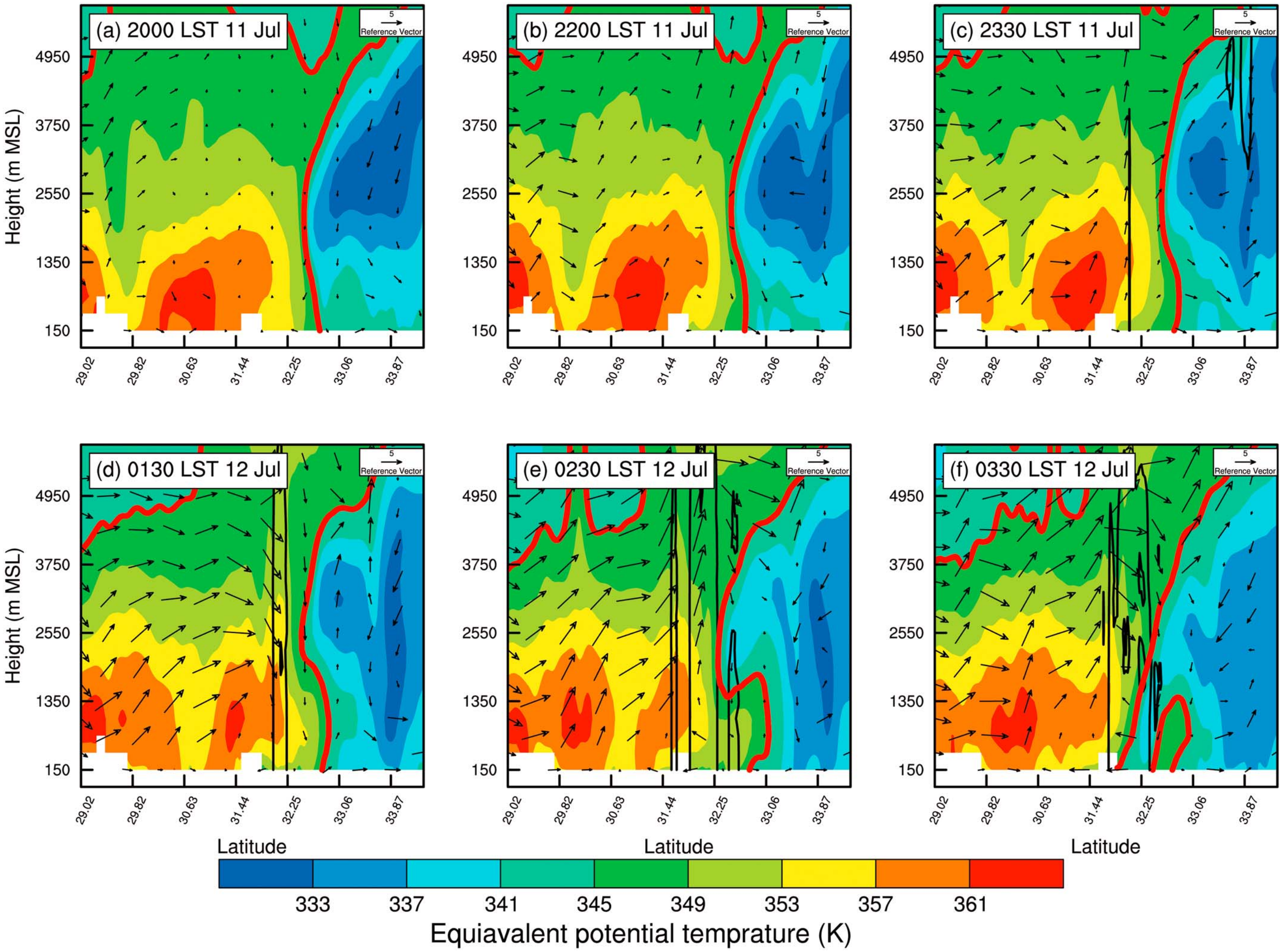

Figure 5. Cross sections along the black line in Figure 4a. The coordinates of the *x* and *y* axes are latitude and vertical height (unit: m) above mean sea level (MSL), respectively. Equivalent potential temperature (shading, unit: K; the 345-K contour is represented by thick, red lines), winds along each cross section (meridional winds, 10× the vertical velocity, vectors, and reference vectors are marked at the upper right, unit: m/s), and contours of radar reflectivity exceeding 30 dBZ (thick black contours, unit: dBZ) are plotted. The time of each subfigure is marked at the upper left. The white blank near surface represents terrain.

An interesting fact is that the squall line did not seem to be directly initiated by the SWV (the center of the SWV was around 108°E at 2300 LST on 11 July in Figure 3c, and the squall line was more than 400 km to the east of the center of the SWV, away from the range of the SWV) but was closely associated with the convergence line to the east of the SWV. The detailed initiation mechanism of this squall line is described below.

4. Convection Initiation Mechanism Analysis Based on VDRAS Output

4.1. Convection Initiation Mechanism

Figure 4 shows the composite reflectivity of the VDRAS analyses. The location and patterns of radar echoes in the VDRAS analyses matched well with those in observation (Figure 1), despite the relatively weaker intensity than observation, which may be attributable to the simplicity of the adjoint cloud model of the VDRAS system (Sun et al., 2010).

To illustrate the vertical structure of the Meiyu Front, vertical cross sections through the location where the squall line formed are shown in Figure 5. The dense contours of equivalent potential temperature show the Meiyu Front zone, and the 345-K contour represents the approximate location of the Meiyu Front. The Meiyu Front was almost vertical, especially in the elevations between 1 and 3 km. Convective initiation of the squall line occurred on the warm side of the Meiyu Front, where lower levels of the troposphere were

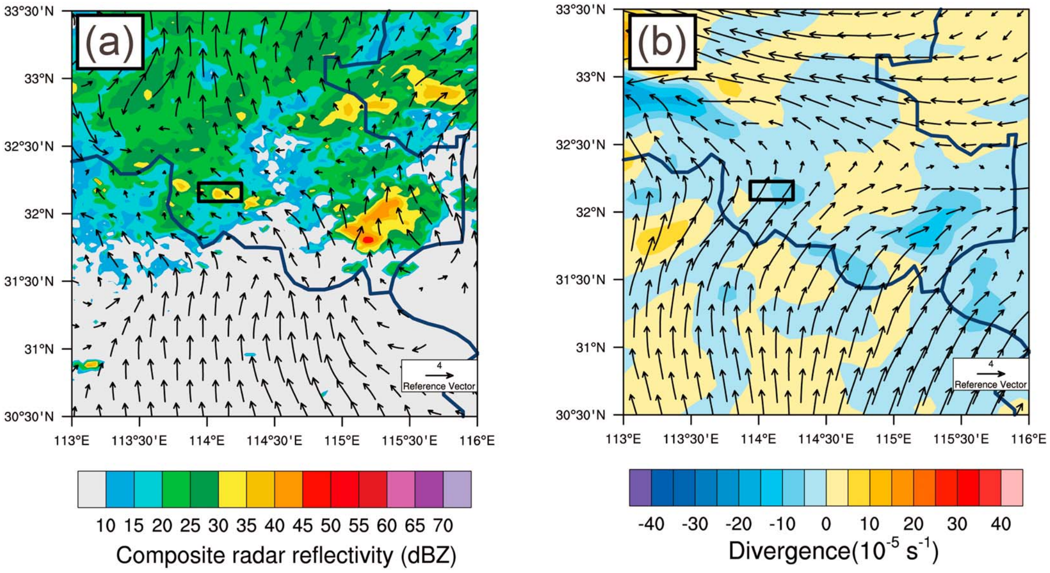

Figure 6. Comparison of wind fields at the levels of 450 and 1,950 m at 2330 LST on 11 July 2014. Composite radar reflectivity (shading, unit: dBZ) and winds at the 450-m level (vectors, unit: m/s) are plotted in (a), and winds at 1,950-m level (vectors, unit: m/s) and divergence (shading, unit: 10^{-5}/s) are plotted in (b). The black boxes in (a) and (b) represent the location where the squall line initiated.

occupied by warm, moist air before the initiation of the squall line (with high equivalent potential temperature; Figures 5a–5c). The air with maximum equivalent potential temperature was at about 1 km (mean sea level, MSL; all heights in this paper are MSL unless otherwise stated). Air with high equivalent potential temperature was located above cooler air near the surface, forming a stable layer below 1 km. This vertical structure inhibited convection near the surface and was favorable for elevated convection. Another important fact apparent in the cross section is the intensification of southerly winds. The southerly winds were very weak at 2000 LST (Figure 5a), but gradually intensified before the initiation of the squall line at 2330 LST on 11 July (Figures 5a–5c), especially above the 1-km level. The effect of this process in the initiation of the squall line will be analyzed in section 4.3.

At 2330 LST, when the squall line was initiated, convergence was not obvious near the surface layer where the squall line formed (Figure 6a), but a convergence line did exist at the level of about 2 km (Figure 6b). This convergence line corresponded well with that observed in the synoptic background to the east of the SWV, described in section 3 and, thus, was closely associated with large-scale convergence. According to the variation of convergence with time and height (Figure 7a), before the formation of the squall line, there was strong convergence at the height of 1.5–3 km, and the surface layer was dominated by divergence. There was a cooling process below around 900 hPa before 2300 LST, which was likely due to radiative cooling near the surface, as shown in the sounding (blue, green, yellow, and orange solid lines in Figure 8). This cooling process led to a stable boundary layer. After 2300 LST, cooling extended to about 700 hPa (orange and red lines in Figure 8). As radiative cooling mainly occurred near surface layer, the cooling below 700 hPa may be attributed to evaporative cooling when convection began to initiate. The dry lower atmosphere before CI was also favorable for evaporative cooling. Below 5 km, humidity increased before CI, and this increase coincided with increasing convective available potential energy (CAPE) and deceasing convective inhibition (CIN; Figures 7c and 7e). For the air parcel of each level, the CAPE is the amount of energy the air parcel would have if lifted from the level of the air parcel through the atmosphere. Similarly, the CIN is the amount of energy the air parcel has to overcome if lifted from the level of the air parcel to the level of free convection. Here the temperature and moisture of air parcels are averaged over a 500-m depth. Therefore, the squall line was probably initiated by convergence above the boundary layer and thus may be deemed elevated convection.

Trajectory analysis provided additional evidence of elevated convection. Applications of trajectories in meteorology and the environmental sciences have been common for some time (Draxler & Hess, 1998; Schumacher, 2009; Stohl, 1998). The reader can refer to the above literature for a description of the

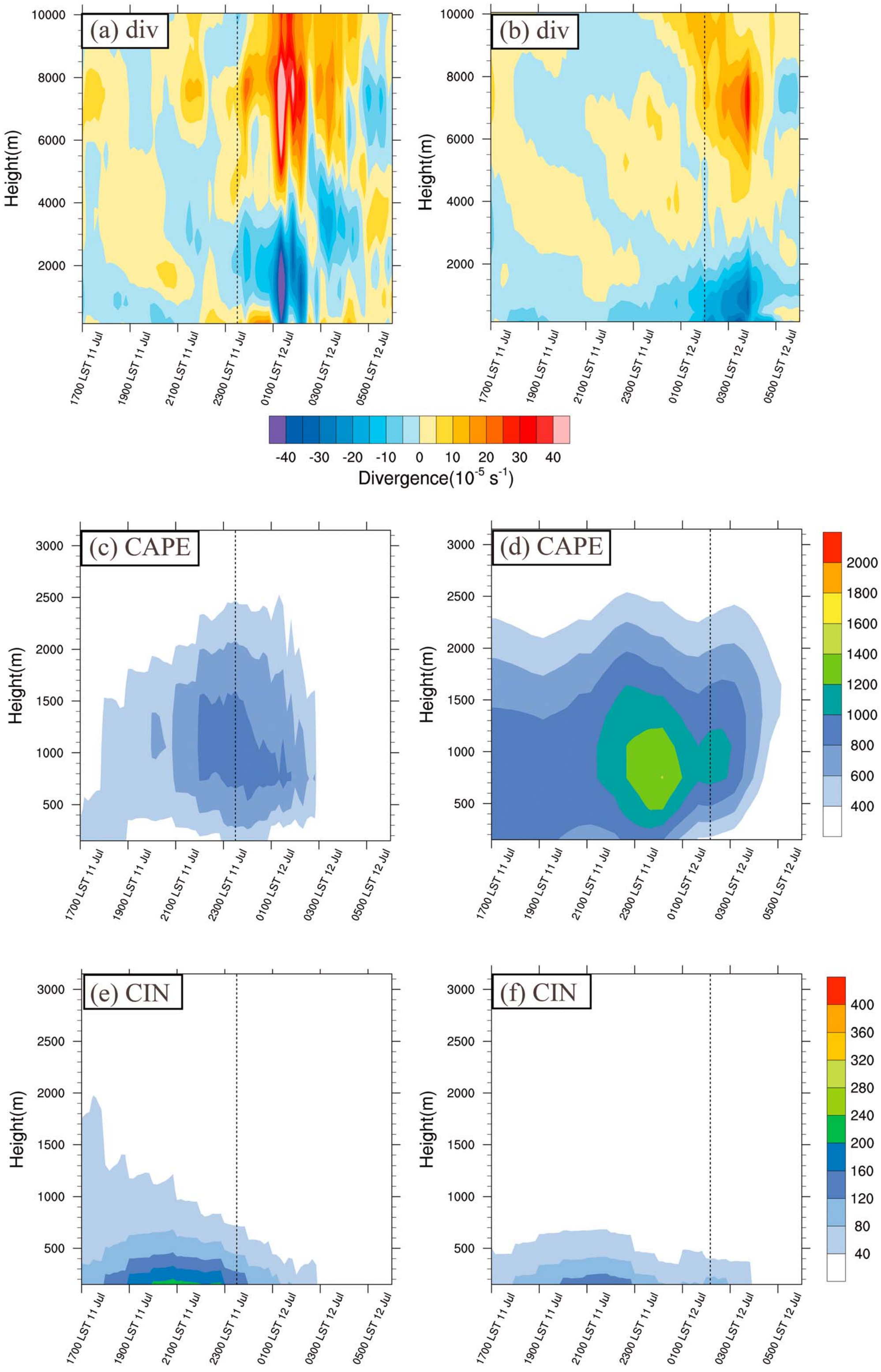

Figure 7. Variation of vertical profiles with time at the locations (a, c, and e) where the squall line first initiated (averaging over the box in Figure 6) and (b, d, and f) where new cells first initiate when the jump propagation occurred (averaging over Box 2 in Figure 4c) on 11–12 July 2014. (a and b) Variation of divergence with height and time (shading, unit: 10^{-5}/s). (c and d) Variation of CAPE with height and time (unit: J/kg). (e and f) Variation of CIN with height and time. The dashed lines represent the time when the squall line initiated (a, c, and e; 2330 LST 11 July) and when new cells began to initiate when the jump propagation occurred (b, d, and f; 0200 LST 12 July).

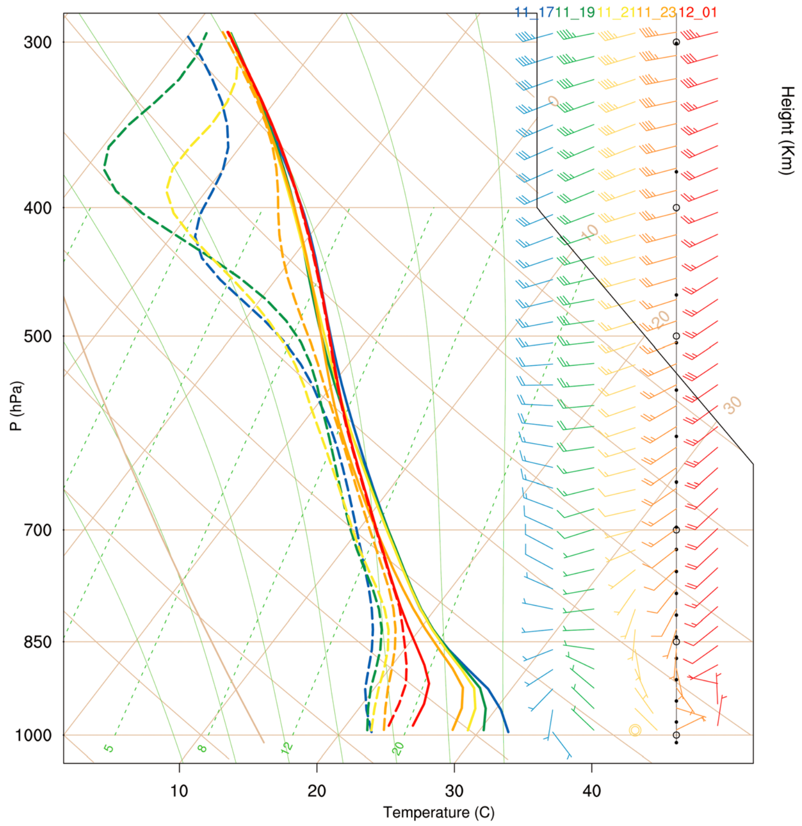

Figure 8. Variation of soundings with time averaging over the box in Figure 6 on 11–12 July 2014. The blue, green, yellow, orange, and red lines and wind barbs (a full wind barb represents wind of 4 m/s, unit: m/s) represent soundings simulated by VDRAS from 1700 LST 11 July to 0100 LST 12 July at 2-hr interval, respectively. The dashed lines represent dew point temperature, and the solid lines represent temperature (unit: °C).

basic principle of trajectory calculation. Backward trajectories of air parcels along the squall line at the level of 1,950 m before the initiation of the squall line showed that the air parcels originated from the level of approximately 1 km, where the equivalent potential temperature reached its maximum in the vertical direction (black lines in Figure 9). In contrast, air parcels near the surface came from the north, where the equivalent potential temperature was lower (white lines in Figure 9). Therefore, the unstable air did not originate from the surface but from 1 km MSL, proving that the convection in the squall line was elevated.

In conclusion, the squall line occurred on the warm side of the Meiyu Front, and a stable surface layer probably resulting from radiative cooling was observed. The initiation of the squall line was driven by convergence above the boundary layer; thus, the convection can be regarded as elevated convection.

4.2. Momentum Budget Analysis

As discussed in section 3, the squall line of interest was initiated before the arrival of the SWV and to the east of it. However, the question of why the squall line was initiated at that particular location and time has yet to be answered. We attempted to provide an answer to this question below.

Figure 10 shows the evolution of the convergence line at the level of 2 km. Before the initiation of the squall line, there was a convergence line of northerly and southerly winds (Figures 10a and 10b). The boxes in Figure 10 mark a region to the south of the squall line of interest. In Figure 10a, westerly winds dominated the region in the box, where air from the south and north converge. Southerly winds then gradually intensified before initiation of the squall line in the box (Figures 10a–10c). With the intensification of southerly winds, the convergence became stronger (Figure 10c; corresponding to convergence near a height of 2 km in Figure 7a), which led to the initiation of the squall line at 2330 LST on 11 July. At 0200 LST on 12

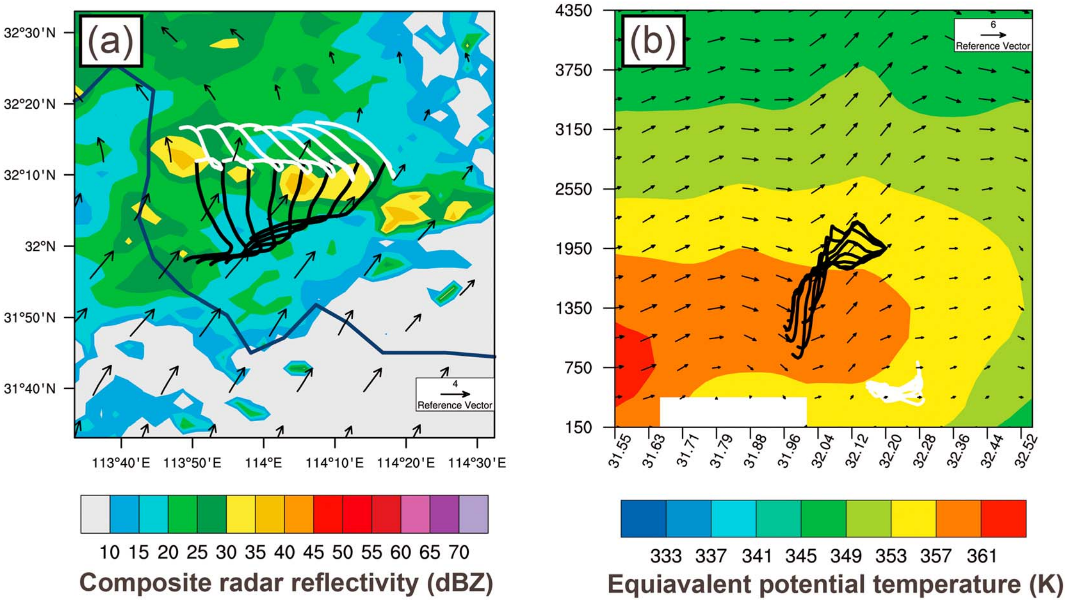

Figure 9. Backward trajectories of air parcels at the levels of 1,950 m (black lines) and 450 m (white lines) along the squall line tracked back from 2300 LST 11 July to 1700 LST 11 July. (a) Horizontal trajectories (thick black and white lines), wind fields at 1,950 m (vector, unit: m/s), and composite radar reflectivity (shading, unit: dBZ) at 2330 LST 11 July. (b) Vertical trajectories projected onto the cross-section of 114° E at 2330 LST 11 July. Variables plotted in (b) are equivalent potential temperature (shading, unit: K) and winds along the cross-section (meridional winds, 10× the vertical velocity, vectors, and reference vectors, are marked at the upper right, unit: m/s). The coordinates of the *x* and *y* axes in (b) are latitude and vertical height (MSL, unit: m), respectively.

July, the speed of the southerly winds reached a maximum, and the winds gradually became southwesterly winds (Figures 10d–10f).

Figure 11 provides momentum budget analyses of the average meridional winds in the boxes of Figure 10 at 1,950-m level. In the height coordinate of VDRAS, the meridional momentum equation takes the following form:

$$\frac{\partial v}{\partial t} = -\left(u\frac{\partial v}{\partial x} + v\frac{\partial v}{\partial y}\right) - w\frac{\partial v}{\partial z} - \frac{1}{\rho}\frac{\partial p}{\partial y} - \mathrm{fu} + F_y \tag{1}$$

In equation (1), $\frac{\partial v}{\partial t}$ is the meridional wind speed tendency, $-\left(u\frac{\partial v}{\partial x} + v\frac{\partial v}{\partial y}\right)$ is the horizontal advection term of the meridional wind, $-w\frac{\partial v}{\partial z}$ is the vertical advection term, $-\frac{1}{\rho}\frac{\partial p}{\partial y}$ is the pressure gradient term, $-\mathrm{fu}$ is the Coriolis force term, and F_y is the residual term, which is obtained by subtracting the other terms on the right side of the equation from the left side and includes the effects of friction and subgrid scale transport. The average meridional wind over the region was very small at 1700 LST on 11 July (Figure 11). By 2100 LST, the meridional winds began to increase gradually. The meridional wind speed tendency reached its maximum at about 2330 LST, when the squall line was initiated. The meridional wind speed reached its maximum at 0200 LST on 12 July, when the squall line matured and then began decaying. The increase in southerly winds corresponded well with the intensification of the convergence shown in Figure 7a. Further analysis of each term on the right side of the equation reveals that the pressure gradient term was the main contributor to the total tendency of meridional wind speed before the initiation of the squall line (2330 LST 11 July, marked by the vertical dashed line in Figure 11). The increasing pressure gradient led to a rapid increase in meridional wind speed. The magnitudes of the other terms including residual term are less than that of pressure gradient term. After the initiation of the squall line (2330 LST 11 July), the contribution of the residual term became much larger, but its magnitude was still less than that of the pressure gradient term before 0200 LST 12 July, so the total tendency of meridional winds remained positive, and the meridional wind speeds kept increasing. At about 0200 LST, the positive tendency of pressure gradient term was offset by the negative tendency of residual term, vertical advection term, and Coriolis force term combined together. The total

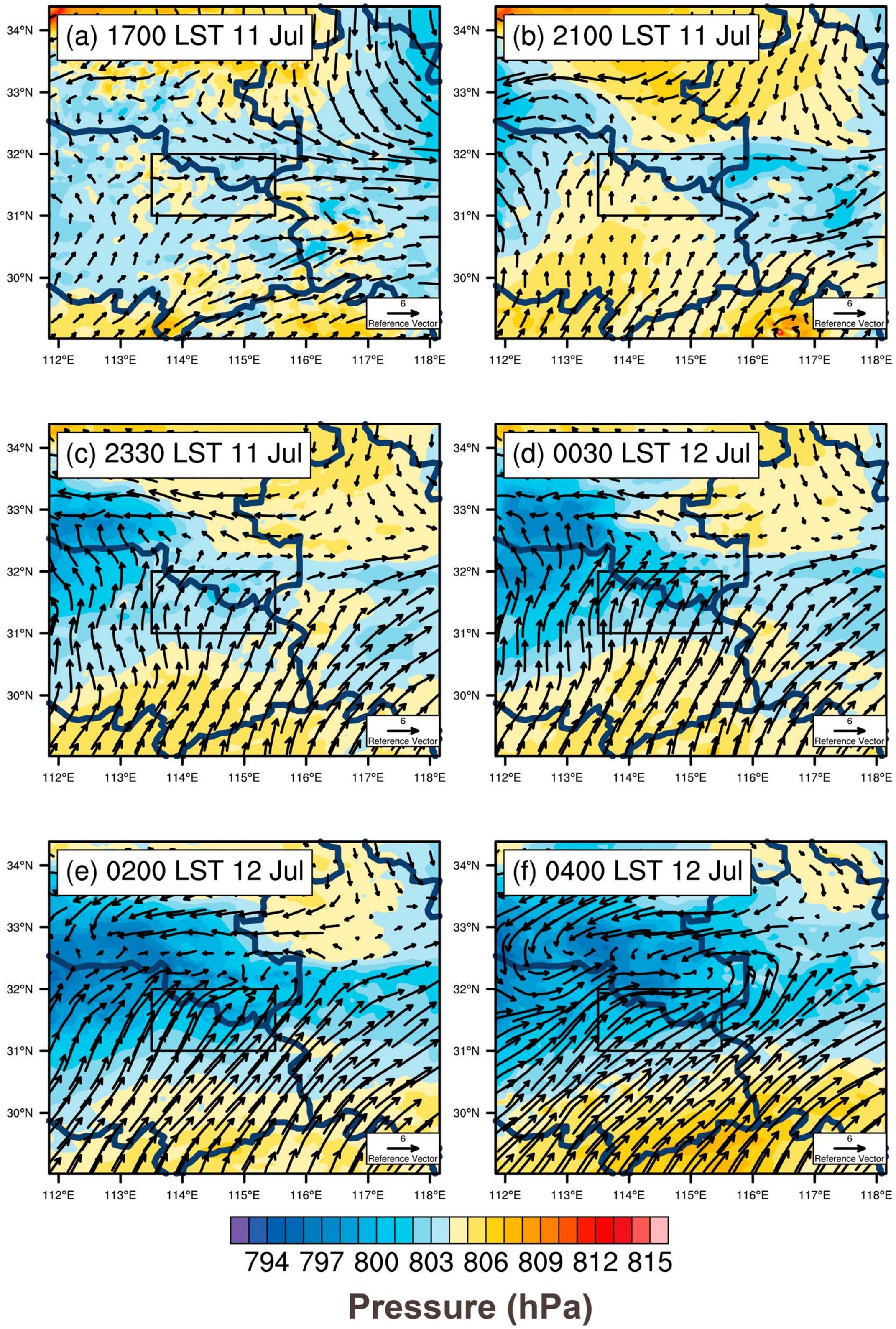

Figure 10. Evolution of the wind (vectors, unit: m/s) and pressure (shading, unit: hPa) fields at 1,950 m. The time of each subfigure is marked at the upper left. The box in each subfigure represents the region for momentum analysis.

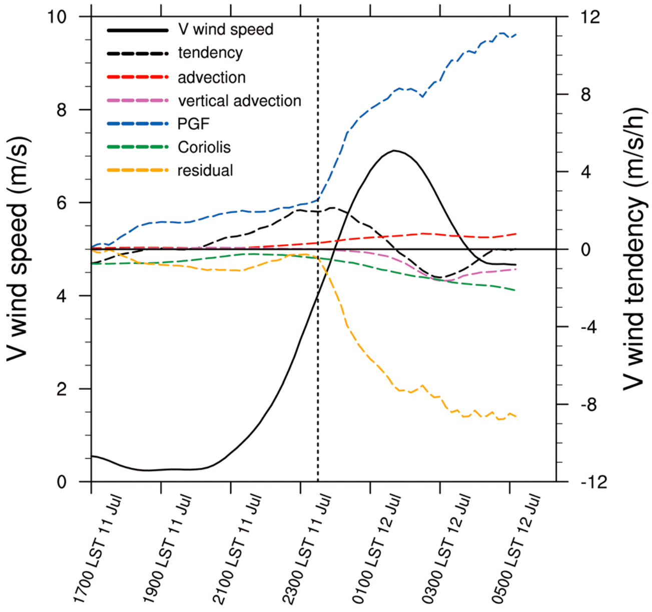

Figure 11. Evolution of meridional wind speed (V wind speed, black solid lines, unit: m/s; the tick marks are on the left *y* axis) and each term in the meridional momentum equation (dashed lines, unit: m/s/hr; the tick marks are on the right *y* axis) averaged in the boxes of Figure 10 at 1,950-m level. The black, red, purple, blue, green, and orange dashed lines represent the tendency of meridional wind (tendency), the horizontal advection term (advection), the vertical advection term (vertical advection), the pressure gradient force term (PGF), the Coriolis force term (Coriolis), and the residual term (residual), respectively. The black dashed vertical line marks the time when the squall line initiated (2330 LST 11 July).

tendency then became negative, so the meridional winds began decreasing. As the vertical motion is often underestimated in VDRAS (Sun et al., 2010), there may be some uncertainties in the vertical advection term. However, these uncertainties did not affect our conclusion pertaining to CI mechanism because the vertical motion was usually weak before CI and the meridional wind speed tendency was dominated by pressure gradient term. Therefore, it is concluded that before the initiation of the squall line, the increase in the pressure gradient force term led to the enhancement of southerly winds to the south of the squall line, which intensified the convergence and initiated the squall line.

The mechanism of the increase of the pressure gradient force term is illustrated in Figure 10. To the west of the location where the squall line formed, there was a preexisting vortex, which corresponds well with the SWV in Figure 3. With the slow eastward movement of the vortex, the subtropical high to the south also strengthened, so the pressure gradient in the south-north direction strengthened between the subtropical high and the vortex, which contributed to the enhancement of southerly winds and the initiation of the squall line.

4.3. Mechanism of Jump Propagation of the Squall Line

In this section, the mechanism of jump propagation, shown in Figure 1, is explored. During the initiation stage of the squall line, cold pools generated by upstream convection were to the west, and the initiation of the squall line was driven mainly by convergence above the boundary layer (Figures 12a and 12c). As the squall line matured, the temperature near surface decreased and the cold pool near surface gradually strengthened (Figure 12d). Then the outflows intensified and converged with warm air from the south. It could also be seen in the cross sections that the cold pool strengthened and expanded toward the south after 2330 LST 11 July (from Figures 5c–5e near surface layer between 31.44°N and 32.25°N). However, the convergence line at the level of 1,950 m remained at the same location as before (Figure 12b). The variation of divergence, CAPE, and CIN with time and height at the location where new cells first initiated are shown in Figures 7b, 7d, and 7f. When the jump propagation occurred, convergence strengthened significantly near the surface (Figure 7b). The CIN was moderate near the surface and became zero above 500 m (Figure 7f). The height of the largest CAPE in Figure 7d also decreased compared with Figure 7c, making it easier to initiate convection near surface. After the initiation of new squall line, the original squall line slowly dissipated to stratiform echoes with the accumulation of cold air and the consumption of CAPE. Therefore, the squall line jumped from the location of the convergence line above the boundary layer to the front of the surface cold pools. During the process, the elevated convection driven by the convergence line above the boundary layer transitioned to surface-based convection driven by surface cold pools.

Therefore, different from the work of Fovell et al. (2006), in which gravity waves ahead of the cold-pool-driven storm were responsible for the discrete propagation, the squall line in this work was driven by convergence line above boundary layer, and the transition to surface-based convection was responsible for the jump propagation. The strengthening of the cold pools was the key factor in this transition. To further understand its mechanism, the temperature budget analysis is shown below.

In height coordinate, the thermodynamic equation could be transformed into the following form:

$$\frac{\partial \boldsymbol{T}}{\partial \boldsymbol{t}} = -\left(\boldsymbol{u}\frac{\partial \boldsymbol{T}}{\partial \boldsymbol{x}} + \boldsymbol{v}\frac{\partial \boldsymbol{T}}{\partial \boldsymbol{y}}\right) - (\Gamma_{\boldsymbol{d}} - \Gamma)\boldsymbol{w} + \frac{\mathbf{1}}{\boldsymbol{c_p}}\frac{\boldsymbol{dQ}}{\boldsymbol{dt}} \tag{2}$$

In equation (2), $\frac{\partial \boldsymbol{T}}{\partial \boldsymbol{t}}$ is the temperature tendency, $-\left(\boldsymbol{u}\frac{\partial T}{\partial x} + v\frac{\partial T}{\partial y}\right)$ is the temperature advection term, $-(\Gamma_d - \Gamma)w$ is the convective term, and $\frac{1}{c_p}\frac{dQ}{dt}$ is the diabatic heating term. Where $\Gamma_{\boldsymbol{d}} = \frac{\boldsymbol{g}}{\boldsymbol{c_p}}$ is the dry adiabatic lapse rate (g is

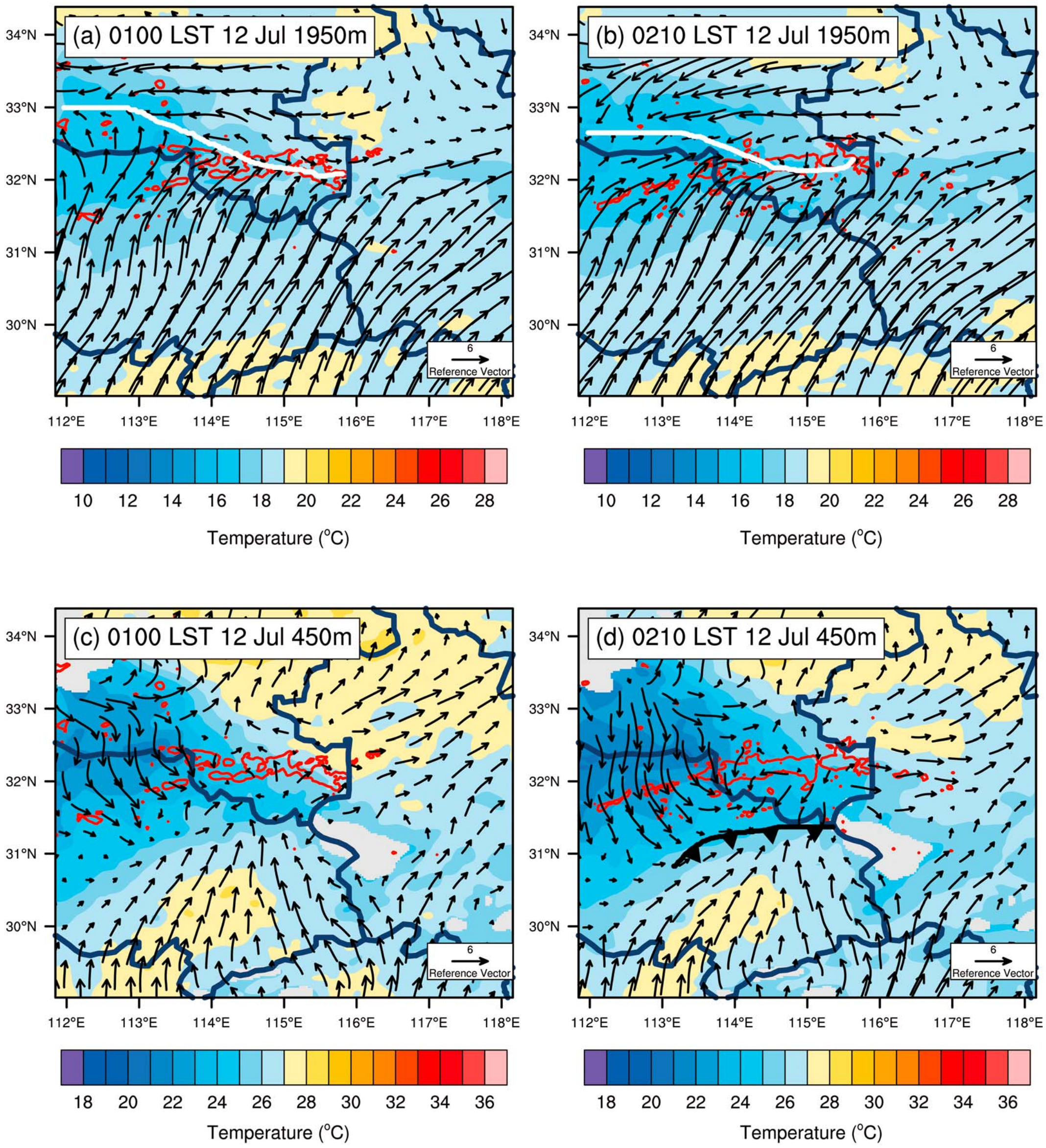

Figure 12. Temperature distribution (unit: °C) and wind (unit: m/s) at the levels of 450 and 1,950 m at 0100 and 0210 LST on 12 July 2014. The red lines represent 35 dBZ contours. The front symbol in (d) represents the outflow boundary of near-surface cold pools. The white solid lines in (a) and (b) represent the convergence line at the height of 1,950 m.

the gravity acceleration and c_p is the specific heat capacity at constant pressure) and $\Gamma = -\frac{\partial T}{\partial z}$ is the lapse rate. Each term in the equation can be calculated from the output of VDRAS except the diabatic heating term, which was obtained by subtracting the other term on the right-hand side from the temperature tendency. The diabatic heating term includes three different effects: turbulent mixing, radiative forcing, and latent heating or cooling (Hu et al., 2014; Vosper et al., 2014). However, we cannot get the contribution of each effect in diabatic heating directly because they are not in the VDRAS output. Besides, in data assimilation, the final analysis is the combination of background (forecast of model) and increments between background and observations (Kalnay, 2003). Those increments may include the contributions of all the terms on the right-hand side of the equation, which are unknown to us. Therefore, the contribution of each effect in diabatic heating cannot be derived from the model. Here we would just see their overall effects and infer their possible contributions.

Figure 13a shows the evolution of temperature and each term in the temperature tendency equation averaged over Box 1 in Figure 4c at 450-m level. The temperature over the box kept decreasing during the

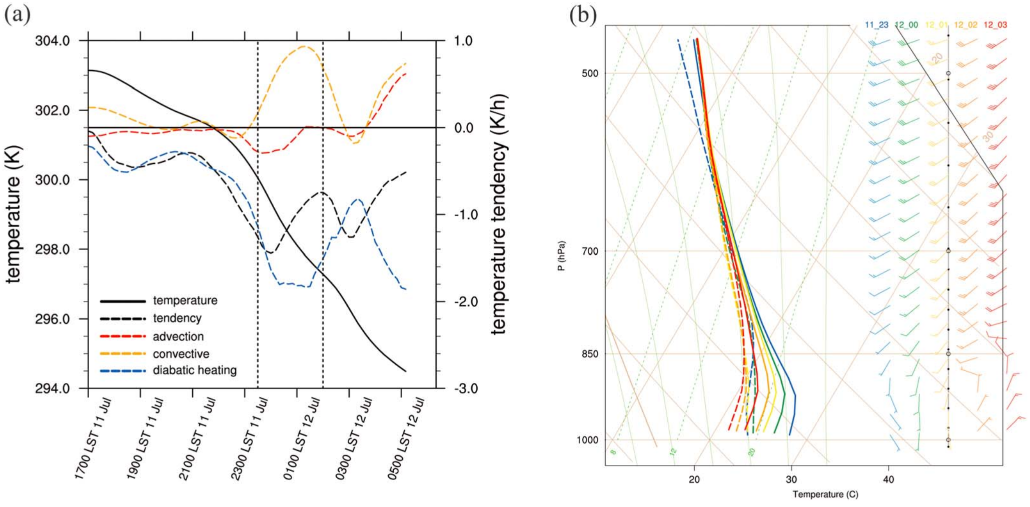

Figure 13. (a) Evolution of temperature (black solid lines, unit: K; the tick marks are on the left *y* axis) and each term in the temperature tendency equation (dashed lines, unit: K/hr; the tick marks are on the right *y* axis) averaged over Box 1 in Figure 4c at 450-m level. The black, red, orange, and blue dashed lines represent the tendency of temperature (tendency), the horizontal advection term (advection), the convective temperature term (convective), and the diabatic heating term (diabatic heating), respectively. The black dashed vertical lines represent the time when the squall line first initiated (2330 LST 11 July) and when the jump propagation began (0210 LST July). (b) Variation of soundings with time averaging over Box 1 in Figure 4c on 11–12 July 2014. The blue, green, yellow, orange, and red lines and wind barbs (a full wind barb represents wind of 4 m/s, unit: m/s) represent soundings simulated by VDRAS from 2300 LST 11 July to 0300 LST 12 July at 1-hr interval, respectively. The dashed lines represent dew point temperature and solid lines represent temperature (unit: °C).

entire night. The wind tendency reached the minimum after the initiation of the squall line at 2330 LST 11 July, meaning the temperature decreased most quickly at that time and the cold pools gradually strengthened. After 2330 LST 11 July, the contribution of diabatic heating term increased significantly, leading a cooling effect near surface, and it was the main contributor of temperature tendency. Due to the probably high cloud cover after CI, the contribution of radiative forcing effect might be small. Besides, as shown in the soundings in Figure 13b, the lower atmosphere was fairly dry before the jump propagation, which was favorable for evaporative cooling. So it may be inferred that the evaporative cooling made the main contribution in the cooling effect. As a result of the evaporative cooling effect, the temperature of the lower atmosphere gradually decreased and the relative humidity increased (Figure 13b). The contribution of the advection term was relatively small, leading to slightly cooling effect after the squall line initiated. The convective term became positive after the initiation of squall line, indicating that the downdrafts from the mature convection had a heating effect. In conclusion, the strengthening of the cold pool can be attributed to diabatic heating (most likely evaporative cooling).

The backward trajectory of the air parcels provides additional evidence of this transition. Compared with Figure 9, the backward trajectory of the air parcels in the newly formed squall line at 0230 LST on 12 July shows that these parcels rose from the near-surface layer, so the convection at this time was more likely to have been surface-based (Figure 14).

5. Conclusion

Previous research has shown that MCSs occur frequently in central East China, and a significant nocturnal peak of MCSs has been observed in the warm season over this region (He et al., 2016). Whether these MCSs are associated with elevated convection is an interesting question that had remained unanswered due to limited observations. Fortunately, during the IOP8 of the Chinese 973 program OPACC, a nocturnal elevated squall was captured during the field campaign. The intense surface and radar observations enabled us to study the detailed mechanism of CI. Based on the observation and analyses from VDRAS, the CI mechanism of a nocturnal squall line along the Meiyu Front over central East China was explored. The synoptic background, mechanisms of initiation, and jump propagation of the squall line are summarized in a schematic diagram (Figure 15).

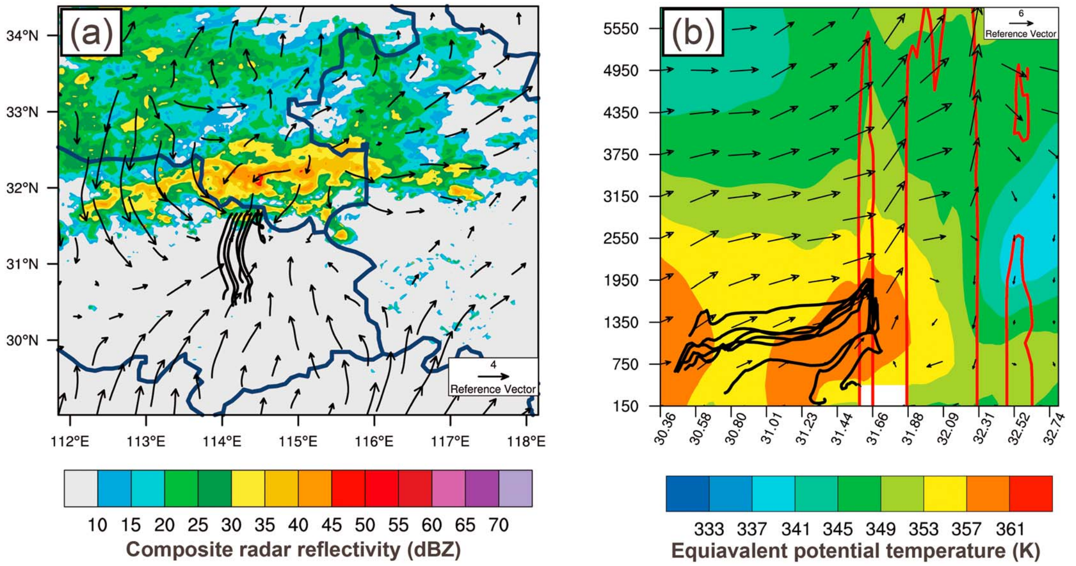

Figure 14. Backward trajectories of air parcels at 1,950 m in front of the squall line tracked back from 0230 LST 12 July to 1700 LST 11 July. (a) Horizontal trajectories (black lines), wind fields at 450 m (vector, unit: m/s), and composite radar reflectivity (shading, unit: dBZ) at 0230 LST 12 July. (b) Vertical trajectories (black lines) projected onto the cross-section of 114.3°E at 0230 LST 12 July. Variables plotted in (b) are equivalent potential temperature (shading, unit: K), winds along the cross section (meridional winds, 10× the vertical velocity, vectors, and reference vectors, are marked at the upper right, unit: m/s) and composite radar reflectivity larger than 30 dBZ (red thick contours).

Figure 15a shows the synoptic background of the squall line. The squall line occurred on the warm side of the Meiyu Front and on the northeastern edge of the subtropical high at night (the brown star in Figure 15a). A SWV was approaching from the upstream region to the west. The advection of the SWV and the strengthening of the subtropical high increased the north-south pressure gradient. The temperature near surface layer decreased before initiation of the squall line, forming a stable boundary layer (Figure 15b). The increasing

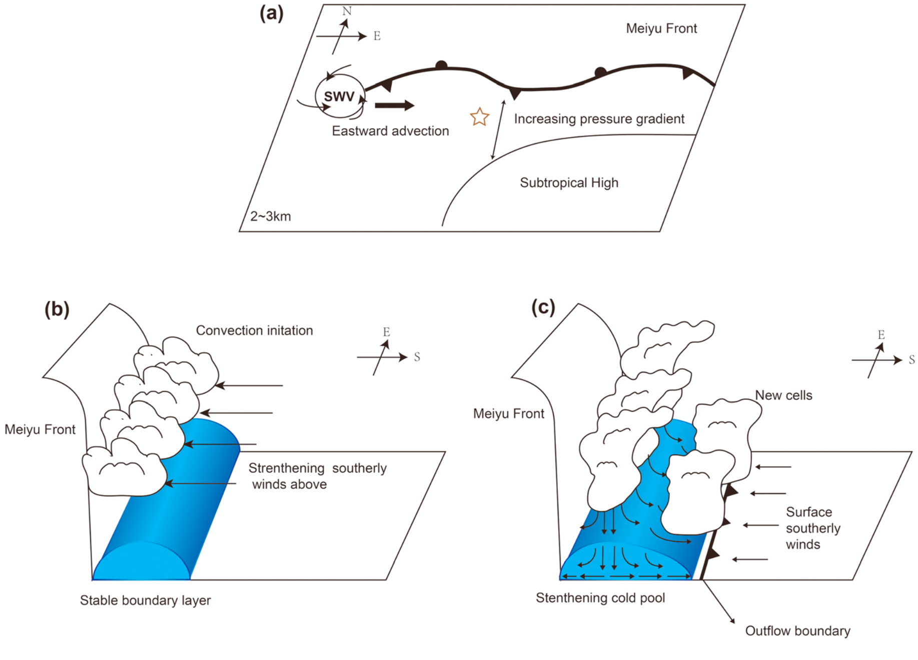

Figure 15. Schematic diagram of the (a) synoptic background, (b) CI mechanism, and (c) the mechanism of jump propagation of the squall line. See text for further information.

pressure gradient led to an increase in the southerly wind speeds above the boundary layer. Thus, the convergence strengthened, resulting in the initiation of the squall line.

A jump propagation occurred when the squall line matured (Figure 15c). This phenomenon occurred due to the development of cold pools that resulted from diabatic heating. The outflows of the cold pool converged with warm air from the south, which initiated new convection in front of the surface cold pools and formed a new squall line. During this process, the squall line transitioned from elevated convection to surface-based convection.

To our knowledge, this study is the first investigation of elevated convection along the Meiyu Front in China. Different from previous research studies of elevated convection in which mesoscale features, as waves or bores, played an important role in initiating and maintaining new convection (Browning et al., 2010; Marsham et al., 2010, 2011; Parker, 2008; Schumacher, 2009; Schumacher & Johnson, 2008), this work showed how the initiation of elevated convection was associated with large-scale convergence and how the structure and evolution of the squall line were affected by the transition from elevated convection to surface-based convection.

The convection environment of central East China has been shown to be different from that of the United States, at the same latitude, by many previous studies (Meng et al., 2013; L. Zheng et al., 2013). The elevated convection of this study demonstrated different characteristics and a different mechanism from elevated convection in the United States. Whether the features of the elevated convection found in this work prevail in central East China requires additional research in the future, including more cases and statistical studies.

Acknowledgments

This study was supported by the Chinese 973 Program 2013CB430104 and the Chinese National Science Foundation under grant 41330421 from the Ministry of Science and Technology of the People's Republic of China (MOST), and the observation data were all collected from the field campaign of this program, and can be made available upon request. The authors sincerely acknowledge the foundation and support of this program. The NCEP FNL and ERA 5 reanalysis data are available online (see https://rda.ucar.edu/datasets/ds083.2/ for details of NCEP FNL data and https://www.ecmwf.int/en/forecasts/datasets/archive-datasets/reanalysis-datasets/era5 for details of ERA 5 data). Users can download WRF source code and manuals from their website (http://www2.mmm.ucar.edu/wrf/users/). We would like to thank Juanzhen Sun and NCAR for providing the access to VDRAS. Computing is conducted at Department of Atmospheric and Oceanic Sciences, School of Physics, Peking University where the VDRAS output is stored and can be made available free of charge upon request.

References

Browning, K., Marsham, J., Nicol, J., Perry, F., White, B., Blyth, A., & Mobbs, S. (2010). Observations of dual slantwise circulations above a cool undercurrent in a mesoscale convective system. *Quarterly Journal of the Royal Meteorological Society*, *136*(647), 354–373.

Chen, X., Zhao, K., Sun, J., Zhou, B., & Lee, W.-C. (2016). Assimilating surface observations in a four-dimensional variational Doppler radar data assimilation system to improve the analysis and forecast of a squall line case. *Advances in Atmospheric Sciences*, *33*(10), 1106–1119. https://doi.org/10.1007/s00376-016-5290-0

Chen, Z., Xu, M., Min, W., & Miao, Q. (2003). Relationship between abnormal activities of southwest vortex and heavy rain the upper reach of Yangtze River during summer of 1998. *Plateau Meteorology*, *22*(2), 162–167.

Colman, B. R. (1990a). Thunderstorms above frontal surfaces in environments without positive CAPE. Part I: A climatology. *Monthly Weather Review*, *118*(5), 1103–1122. https://doi.org/10.1175/1520-0493(1990)118<1103:TAFSIE>2.0.CO;2

Colman, B. R. (1990b). Thunderstorms above frontal surfaces in environments without positive CAPE. Part II: Organization and instability mechanisms. *Monthly Weather Review*, *118*(5), 1123–1144. https://doi.org/10.1175/1520-0493(1990)118<1123:TAFSIE>2.0.CO;2

Corfidi, S. F., Corfidi, S. J., & Schultz, D. M. (2008). Elevated convection and castellanus: Ambiguities, significance, and questions. *Weather and Forecasting*, *23*(6), 1280–1303. https://doi.org/10.1175/2008WAF2222118.1

Crook, N. A., & Moncrieff, M. W. (1988). The effect of large-scale convergence on the generation and maintenance of deep moist convection. *Journal of the Atmospheric Sciences*, *45*(23), 3606–3624. https://doi.org/10.1175/1520-0469(1988)045<3606:TEOLSC>2.0.CO;2

Draxler, R. R., & Hess, G. (1998). An overview of the HYSPLIT_4 modelling system for trajectories. *Australian Meteorological Magazine*, *47*(4), 295–308.

Fovell, R. G., Mullendore, G. L., & Kim, S. H. (2006). Discrete propagation in numerically simulated nocturnal squall lines. *Monthly Weather Review*, *134*(12), 3735–3752.

Fu, S., Sun, J., Zhao, S., & Li, W. (2011). The energy budget of a southwest vortex with heavy rainfall over south China. *Advances in Atmospheric Sciences*, *28*(3), 709–724. https://doi.org/10.1007/s00376-010-0026-z

Geerts, B., Parsons, D., Ziegler, C. L., Weckwerth, T. M., Biggerstaff, M. I., Clark, R. D., et al. (2017). The 2015 plains elevated convection at night field project. *Bulletin of the American Meteorological Society*, *98*(4), 767–786. https://doi.org/10.1175/BAMS-D-15-00257.1

Glickman, T. S., & Zenk, W. (2000). *Glossary of meteorology* (2nd ed.). Boston: Amer. Meteor. Soc.

He, Z., Zhang, Q., Bai, L., & Meng, Z. (2016). Characteristics of mesoscale convective systems in central East China and their reliance on atmospheric circulation patterns. *International Journal of Climatology*, 3276–3290. https://doi.org/10.1002/joc.4917

Horgan, K. L., Schultz, D. M., Hales, J. E., Corfidi, S. F., & Johns, R. H. (2007). A five-year climatology of elevated severe convective storms in the United States east of the Rocky Mountains. *Weather and Forecasting*, *22*(5), 1031–1044. https://doi.org/10.1175/WAF1032.1

Hu, H., Zhang, Q., Xie, B., Ying, Y., Zhang, J., & Wang, X. (2014). Predictability of an advection fog event over North China. Part I: Sensitivity to initial condition differences. *Monthly Weather Review*, *142*(5), 1803–1822. https://doi.org/10.1175/mwr-d-13-00004.1

Jirak, I. L., Cotton, W. R., & McAnelly, R. L. (2003). Satellite and radar survey of mesoscale convective system development. *Monthly Weather Review*, *131*(10), 2428–2449. https://doi.org/10.1175/1520-0493(2003)131<2428:SARSOM>2.0.CO;2

Kalnay, E. (2003). *Atmospheric modeling, data assimilation and predictability*. Cambridge: Cambridge University Press.

Luo, Y., Gong, Y., & Zhang, D.-L. (2014). Initiation and organizational modes of an extreme-rain-producing mesoscale convective system along a Mei-Yu front in East China. *Monthly Weather Review*, *142*(1), 203–221. https://doi.org/10.1175/MWR-D-13-00111.1

Maddox, R. A. (1980). Meoscale convective complexes. *Bulletin of the American Meteorological Society*, *61*(11), 1374–1387. https://doi.org/10.1175/1520-0477(1980)061<1374:MCC>2.0.CO;2

Marsham, J. H., Browning, K. A., Nicol, J. C., Parker, D. J., Norton, E. G., Blyth, A. M., et al. (2010). Multi-sensor observations of a wave beneath an impacting rear-inflow jet in an elevated mesoscale convective system. *Quarterly Journal of the Royal Meteorological Society*, *136*(652), 1788–1812. https://doi.org/10.1002/qj.669

Marsham, J. H., Trier, S. B., Weckwerth, T. M., & Wilson, J. W. (2011). Observations of elevated convection initiation leading to a surface-based squall line during 13 June IHOP_2002. *Monthly Weather Review*, *139*(1), 247–271. https://doi.org/10.1175/2010MWR3422.1

Meng, Z., Yan, D., & Zhang, Y. (2013). General features of squall lines in East China. *Monthly Weather Review*, *141*(5), 1629–1647. https://doi.org/10.1175/mwr-d-12-00208.1

Moore, J. T., Glass, F. H., Graves, C. E., Rochette, S. M., & Singer, M. J. (2003). The environment of warm-season elevated thunderstorms associated with heavy rainfall over the central United States. *Weather and Forecasting*, *18*(5), 861–878. https://doi.org/10.1175/1520-0434(2003)018<0861:TEOWET>2.0.CO;2

Parker, M. D. (2008). Response of simulated squall lines to low-level cooling. *Journal of the Atmospheric Sciences*, *65*(4), 1323–1341. https://doi.org/10.1175/2007JAS2507.1

Parker, M. D., & Johnson, R. H. (2000). Organizational modes of midlatitude mesoscale convective systems. *Monthly Weather Review*, *128*(10), 3413–3436. https://doi.org/10.1175/1520-0493(2001)129<3413:OMOMMC>2.0.CO;2

Reif, D. W., & Bluestein, H. B. (2017). A 20-year climatology of nocturnal convection initiation over the central and southern Great Plains during the warm season. *Monthly Weather Review*, *145*(5), 1615–1639. https://doi.org/10.1175/MWR-D-16-0340.1

Rotunno, R., Klemp, J. B., & Weisman, M. L. (1988). A theory for strong, long-lived squall lines. *Journal of the Atmospheric Sciences*, *45*(3), 463–485. https://doi.org/10.1175/1520-0469(1988)045<0463:ATFSLL>2.0.CO;2

Schumacher, R. S. (2009). Mechanisms for quasi-stationary behavior in simulated heavy-rain-producing convective systems. *Journal of the Atmospheric Sciences*, *66*(6), 1543–1568. https://doi.org/10.1175/2008JAS2856.1

Schumacher, R. S., & Johnson, R. H. (2008). Mesoscale processes contributing to extreme rainfall in a midlatitude warm-season flash flood. *Monthly Weather Review*, *136*(10), 3964–3986. https://doi.org/10.1175/2008MWR2471.1

Skamarock, W. C., Klemp, J. B., Dudhia, J., Gill, D. O., Barker, D. M., Duda, M. G., et al. (2008). A description of the Advanced Research WRF version 3. NCAR Tech. Note NCAR/TN–4751STR (113 pp.).

Stohl, A. (1998). Computation, accuracy and applications of trajectories—A review and bibliography. *Atmospheric Environment*, *32*(6), 947–966. https://doi.org/10.1016/S1352-2310(97)00457-3

Sun, J. (2005). Initialization and numerical forecasting of a supercell storm observed during STEPS. *Monthly Weather Review*, *133*(4), 793–813. https://doi.org/10.1175/mwr2887.1

Sun, J., Chen, M., & Wang, Y. (2010). A frequent-updating analysis system based on radar, surface, and mesoscale model data for the Beijing 2008 forecast demonstration project. *Weather and Forecasting*, *25*(6), 1715–1735. https://doi.org/10.1175/2010waf2222336.1

Sun, J., & Crook, N. A. (1997). Dynamical and microphysical retrieval from Doppler radar observations using a cloud model and its adjoint. Part I: Model development and simulated data experiments. *Journal of the Atmospheric Sciences*, *54*(12), 1642–1661. https://doi.org/10.1175/1520-0469(1997)054<1642:damrfd>2.0.co;2

Sun, J., & Crook, N. A. (1998). Dynamical and microphysical retrieval from Doppler radar observations using a cloud model and its Adjoint. Part II: Retrieval experiments of an observed Florida convective storm. *Journal of the Atmospheric Sciences*, *55*(5), 835–852. https://doi.org/10.1175/1520-0469(1998)055<0835:damrfd>2.0.co;2

Sun, J., & Crook, N. A. (2001). Real-time low-level wind and temperature analysis using single WSR-88D data. *Weather and Forecasting*, *16*(1), 117–132. https://doi.org/10.1175/1520-0434(2001)016<0117:RTLLWA>2.0.CO;2

Tai, S.-L., Liou, Y.-C., Sun, J., Chang, S.-F., & Kuo, M.-C. (2011). Precipitation forecasting using Doppler radar data, a cloud model with Adjoint, and the weather research and forecasting model: Real case studies during SoWMEX in Taiwan. *Weather and Forecasting*, *26*(6), 975–992. https://doi.org/10.1175/waf-d-11-00019.1

Vosper, S. B., Hughes, J. K., Lock, A. P., Sheridan, P. F., Ross, A. N., Jemmett-Smith, B., & Brown, A. R. (2014). Cold-pool formation in a narrow valley. *Quarterly Journal of the Royal Meteorological Society*, *140*(679), 699–714. https://doi.org/10.1002/qj.2160

Weckwerth, T. M., & Parsons, D. B. (2006). A review of convection initiation and motivation for IHOP_2002. *Monthly Weather Review*, *134*(1), 5–22.

Wilson, J. W., & Roberts, R. D. (2006). Summary of convective storm initiation and evolution during IHOP: Observational and modeling perspective. *Monthly Weather Review*, *134*(1), 23–47. https://doi.org/10.1175/MWR3069.1

Wu, N., Lin, L., Feng, Y., Liu, Y., & Zheng, W. (2013). Analysis of elevated thunderstorm process over South China in early spring of 2012 (in Chinese). *Meteorological Monthly*, *39*(4), 410–417.

Xue, M. (2016). Preface to the special issue on the "Observation, prediction and analysis of severe convection of China"(OPACC) national "973" Projec. *Advances in Atmospheric Sciences*, *33*(10), 1099–1101. https://doi.org/10.1007/s00376-016-0002-3

Zhang, Y., Yu, X., Sun, J., Liang, J., & Lv, L. (2014). Analysis of an elevated thunderstorm in Henan Province in the early spring of 2012 (in Chinese). *Meteorological Monthly*, *40*(1), 48–58.

Zheng, L., Sun, J., Zhang, X., & Liu, C. (2013). Organizational modes of mesoscale convective systems over central East China. *Weather and Forecasting*, *28*(5), 1081–1098. https://doi.org/10.1175/waf-d-12-00088.1

Zheng, Y., Chen, J., Ge, G., Huang, Y., & Zhang, C. (2008). Review on the synopic scale Meiyu front system and its synoptics' definition (in Chinese). *Acta Scientiarum Naturalium Universitutatis Pekinensis*, *44*(1), 157–164.